

bioSBM: a random graph model to integrate epigenomic data in chromatin structure prediction

Alex Chen Yi Zhang,^{*} Angelo Rosa,[†] and Guido Sanguinetti[‡]

Scuola Internazionale Superiore di Studi Avanzati (SISSA), Via Bonomea 265, 34136 Trieste, Italy

(Dated: September 24, 2024)

The spatial organization of chromatin within the nucleus plays a crucial role in gene expression and genome function. However, the quantitative relationship between this organization and nuclear biochemical processes remains under debate. In this study, we present a graph-based generative model, bioSBM, designed to capture long-range chromatin interaction patterns from Hi-C data and, importantly, simultaneously link these patterns to biochemical features. Applying bioSBM to Hi-C maps of the GM12878 lymphoblastoid cell line, we identified a latent structure of chromatin interactions, revealing 12 distinct communities that strongly align with known biological annotations. Additionally, we infer a linear transformation that maps biochemical observables, such as histone marks, to the parameters of the generative graph model, enabling accurate genome-wide predictions of chromatin contact maps on out-of-sample data, both within the same cell line, and on the completely unseen HCT116 cell line under RAD21 depletion. These findings highlight bioSBM's potential as a powerful tool for elucidating the relationship between biochemistry and chromatin architecture and predicting long-range genome organization from independent biochemical data.

I. INTRODUCTION

A characteristic feature of a eukaryotic cell, as opposed to archaea and eubacteria, is the sequestration of the cellular genome in a tight cellular space called the nucleus. In humans, the approximately two-meter-long chromatin filament is tightly packed in a nucleus of 5-10 μm in diameter. This packing is highly organized, as demonstrated by immunofluorescence microscopy experiments that show the heterogeneous subnuclear localization patterns of various proteins and histone marks thus hinting at the existence of functionally distinct compartments within the nucleus [1–4].

The advent of Chromatin Conformation Capture (3C) [5], particularly its now popular derivative Hi-C [6], allowed the mapping of chromatin contacts at a genome-wide level. Thanks to the fixation of nuclei with formaldehyde, which preserves information about the spatial proximity of linearly distal DNA loci, Hi-C experiments generate contact frequency maps that display non-trivial interaction motifs. One notable feature of the organization of chromatin unveiled by Hi-C is the segregation of the genome into two classes of domains dubbed A and B compartments, which are characterized by distinct interaction patterns. On top of these connectivity differences, A and B compartments have been shown to correlate with epigenetic marks associated with active (A) and silenced (B) transcriptional states [6]. Despite these correlations, more detailed microscopy studies and information from epigenetics (*e.g.*, histone modifications and preferential binding of transcription factors) [7–9] suggest that the transcriptional state of the genome is more nuanced and the binary classification into A/B

compartments may be excessively oversimplified. While A/B compartments and the sub-compartments defined by Rao *et al.* [9] do provide valuable correlative links between distinct 3D chromatin interaction patterns and different epigenetic marks, a quantitative understanding of the relationship between 3D organization and underlying nuclear biochemical processes remains elusive.

Several attempts to explain the emergence and spatial organization of compartments have invoked polymer-based models, which aim to simulate chromatin structure by incorporating biophysical properties [10–13]. While such models provide valuable insights by connecting some biochemical processes to mechanisms of genome folding, their reliance on polymer simulations results in high computational costs, particularly when additional parameters need to be estimated. In contrast, more recent deep learning models scale efficiently and have achieved impressive success in predicting Hi-C contact maps. Early models make predictions using DNA sequence alone, but these predictions do not account for cell-type-specific variability [14–16]. More recently, deep learning approaches have started to incorporate 1D epigenetic signals [17], improving predictive accuracy across different cellular conditions. However, these models remain largely uninterpretable, making it difficult to connect their predictive power with underlying biological mechanisms.

In recent years, ideas from the field of network or graph theory [18] have emerged as a promising paradigm to study chromatin organization at the mesoscopic level. These methods avoid the computational overheads of microscopic polymer-based models by abstracting chromatin structure as a network of interactions, where DNA loci are treated as nodes and their contacts as edges. Such graph-based approaches not only were successfully used to reveal structural patterns [19, 20] but also provided interpretable insights into the relationship between chromatin architecture and biological function [21–23].

In this paper, we propose bioSBM, an interpretable

^{*} chzhang@sissa.it

[†] anrosa@sissa.it

[‡] gsanguin@sissa.it

network model that directly links chromatin structure with biochemical features. bioSBM is based on the stochastic block model (SBM) [24, 25], a class of generative network models that partition the network into communities based on interaction patterns, making them highly suitable for uncovering latent structures in chromatin interaction maps. bioSBM modulates this community structure by considering biochemical covariates such as histone modifications and transcription factor binding, therefore constructing a quantitative framework to understand the relationship between 3D chromatin organization and biochemical processes. Unlike traditional SBMs, which assign each node to a single community, bioSBM allows for mixed memberships, enabling genomic regions to participate in multiple communities simultaneously, thus capturing the context-dependent nature of chromatin interactions.

We apply our model to Hi-C data from the GM12878 lymphoblastoid cell line, where we identify interpretable community structures that include, but go beyond, the conventional A/B compartmentalization and subcompartments [9]. In addition to community detection, we can infer the map from biochemical features to the community composition of entire chromosomes and we learn the interaction patterns that link the various communities. Finally, the results of our inference allow us to show that bioSBM can serve as a generative model capable of predicting Hi-C maps for unseen chromosomes and cellular conditions, further demonstrating its robustness and utility.

In Section II we provide a detailed overview of the *vanilla* stochastic block model and discuss how it can be adapted to better describe different types of analyzed data. In particular, we provide details of the data we utilize (distance-corrected, or *observed-over-expected*, Hi-C maps) in Sec. II A, and our customized version of the SBM in Sec. II B. Then, in Sec. II C we introduce the main features of the inference algorithm specifically developed to compute posterior probabilities for our model, while leaving the mathematical details of its derivation in the Supplemental Material (SM). We present our main results in Sec. III, demonstrating the biological relevance and predictive power of our bioSBM model. Finally, in Sec. IV we discuss our results in the context of chromosome organization and conclude by highlighting, in particular, possible future applications.

II. MODEL AND METHODS

A. SBM and its generalization

SBMs are a particular class of random graphs. A graph $\mathcal{G} = (\mathcal{V}, \mathcal{E})$ consists of a set of vertices \mathcal{V} , representing entities $1, \dots, N$ and a set of edges $(i, j) \in \mathcal{E} \subset \mathcal{V} \times \mathcal{V}$, denoting pairwise interactions between these entities. Edges can be binary, indicating the presence or the absence of a link, or they can be weighted, reflecting the *strength*

of interactions. Random graphs [26, 27] denote graphs whose structure is itself a random variable, usually as a result of a random attachment process.

SBMs have their roots in the world of social sciences [28, 29], where they were used to model populations divided into sub-populations or *communities*. The central idea is that interactions between individuals are influenced by their community, creating a non-trivial structure in the interaction graph. This simple yet powerful idea made SBMs into popular models to study general types of relational data.

Numerous algorithms have been developed to detect community structures in complex networks and to make sense of them [30, 31]. Box 1 provides a schematic overview of the main ideas behind SBMs and of some of their most common extensions.

In our case, the relational data is derived from Hi-C contact frequency maps. Early Hi-C experiments demonstrated that contact frequency between genomic loci is strongly influenced by *linear proximity* or genomic distance, with the contact probability exhibiting a power-law decay as a function of this distance [6]. This scaling behavior is understood to arise from fundamental polymer physics mechanisms [32–34]. Instead of using raw Hi-C data, it is often more insightful to study the so-called *observed-over-expected* (OE) Hi-C maps. These OE maps are derived as the logarithmic ratio between the actual contact frequencies recorded in Hi-C matrices and the expected contact frequencies based on genomic distances. These maps effectively highlight interaction patterns of chromatin by accounting for and removing the global polymeric effects that contribute to the power-law scaling. Significant interactions can be observed across large genomic scales, sometimes spanning entire chromosomes. To uncover a latent structure in these interaction patterns, we employ a weighted SBM. Namely, to capture the complexity of community structures we use a so-called *mixed membership* version of the SBM (MMSBM, see Sec. II B) that allows the same genomic regions to belong to multiple classes.

B. bioSBM: a covariate dependent MMSBM for long-range chromatin contacts

A key difference between standard relational data and the biological setting we consider is the availability of a wealth of additional data in biology. While Hi-C measures contact patterns between chromosomal regions, a variety of biochemical assays, such as ChIP-seq [35], provide 1D genomic maps of specific epigenomic marks at such regions. In our model, we integrate this ChIP-seq data as a vector of biochemical covariates associated with each node, and which modulates the probability of each node belonging to the different communities.

Formally, bioSBM is a hierarchical Bayesian model [36, 37] over weighted graphs. Graph nodes $i \in \{1, \dots, N\}$ represent a set of contiguous genomic regions of fixed

length. The observed weighted network has adjacency matrix Y , with Y_{ij} representing the logarithmic OE Hi-C contact frequency (Sec. II A) between region i and j . The observed weighted network is assumed to be generated according to the latent distributions of group memberships for each node/genomic region, as well as the matrices that specify group-group interaction strengths. Each node i has an associated membership proportions' vector θ_i , where θ_{ig} denotes the probability of node i belonging

to group g , allowing nodes to belong to multiple classes and display interactions that are context-dependent.

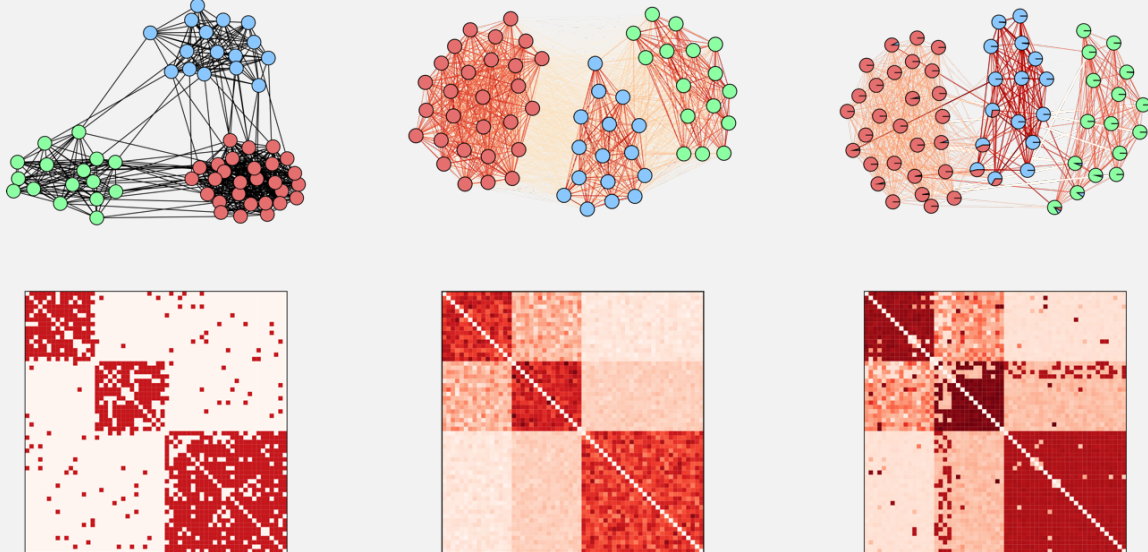
The group-group interaction strengths are defined by matrices B and σ^2 , where B_{gk} and σ_{gk}^2 represent the mean and variance of the strength of interaction between class g and class k . For each pair of nodes (i, j) , discrete variables z_{ij} and z_{ji} denote the group membership of i when interacting with j , and vice-versa.

Box 1: Flavours of Stochastic Block Models (SBM's)

SBM's are a particular type of generative models used in network theory to describe the structure of networks by dividing nodes into communities or blocks. Each block represents a group of nodes that have a similar pattern of connections. The SBM assumes that the probability of a connection between any two nodes depends only on the blocks to which the nodes belong. This model helps understand the network's underlying structure and is commonly used for community detection [28–30]. The generative process defined by an SBM is as follows:

- Determine the number of communities K .
- Assign each node to one of the K communities,
- For each pair of nodes, generate an edge with a probability that depends on the communities of the nodes. Specifically, generate a Bernoulli random variable with the parameter of the distribution depending on the colors of the two nodes.

The left panel of the figure shows a stochastic block model with $K = 3$ communities. In this example, the graph is an *assortative* SBM, meaning that intra-class edge probabilities are higher than inter-class ones.



In its basic version, the SBM is binary, *i.e.* the edges between nodes are either present or absent. However, many real-world networks involve weighted edges, where the connections between nodes have different strengths or capacities. To adapt the binary SBM for valued (weighted) graphs, we can modify the probability distribution of the edges given the colors or communities to which the two involved nodes belong. Instead of a Bernoulli random variable, we might use Poisson random variables for integer value edges, or Gaussian random variables for real-valued networks, specifying the means and variances of the distributions for each pair of distinct communities [38]. The central panel shows an instance of such weighted SBM.

Another aspect we can tweak is the fact that in the traditional SBM, each node belongs to a single community or block. In many networks, nodes may exhibit characteristics of multiple communities. The *mixed membership* SBM (MMSBM) [39] addresses this by allowing nodes to belong to multiple communities by specifying a probability distribution over classes, or membership proportions. In this paper, we will work with an SBM that has real-valued edges and mixed membership proportions. The right panel shows an example of weighted MMSBM.

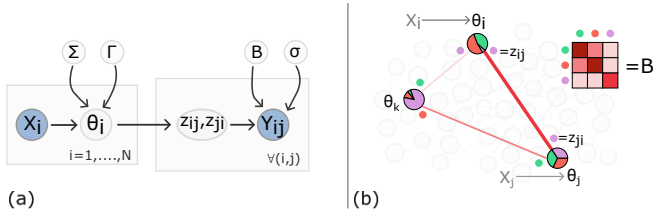


FIG. 1. Generative process of bioSBM. (a) Hierarchical Bayesian model representing the generative process. The colored circles represent observed variables, which are the edge weights Y_{ij} and the node covariates vectors x_i . The connectivity patterns of the graph are determined by per-node latent class membership vectors θ_i and global hyperparameters represented by the circles outside the rectangles. (b) An example displays the sampling for the weights of edges between a subset of three nodes.

The edge weight is then sampled from a Gaussian distribution parameterized by B and σ^2 matrices. Putting everything together, the generative process for bioSBM proceeds as follows:

- Each node has an associated vector of P features x_i , with $X \in \mathbb{R}^{P \times N}$ denoting the covariate matrix. The covariates correspond to biochemical data that can be associated with the different genomic regions, such as data from ChIP-seq assays.
- For every node i we sample a distribution θ_i from the logistic normal distribution [40, 41] with mean $\mu_i = \Gamma(x_i)$ and global covariance Σ

$$\eta_i \sim \mathcal{N}_K(\Gamma(x_i), \Sigma) \quad (1)$$

$$\theta_{ik} = \frac{\exp(\eta_{ik})}{\sum_{k'=1}^K \exp(\eta_{ik'})} \quad (2)$$

$\Gamma: \mathbb{R}^P \rightarrow \mathbb{R}^K$ is the parametric function that maps biochemical features to probabilities over group memberships. In our specific implementation, Γ is simply a linear transformation encoded in a $K \times P$ matrix. Notice that Γ and Σ are global parameters shared among all nodes.

- For every pair of nodes (i, j) with $i = 1, \dots, N$ and $j = 1, \dots, i - 1$

$$z_{ij} \sim \text{Mult}(\theta_i) \quad z_{ji} \sim \text{Mult}(\theta_j) \quad (3)$$

with z_{ij} being the membership of node i interacting with node j and vice-versa, sampled from the multinomial distribution with probabilities θ_i and θ_j respectively.

- Once the memberships of i and j are sampled the weight of the edge is sampled from a Gaussian of which parameters are encoded in the global B and σ matrices.

$$P(Y_{ij}|z_{ij} = k, z_{ji} = g, B, \sigma) = \mathcal{N}(Y_{ij}|B_{kg}, \sigma_{kg}) \quad (4)$$

Schematically, the bioSBM model is represented as a graphical model as in Fig. 1.

C. Posterior inference

To uncover the latent structure of chromatin interactions, we developed a posterior inference algorithm tailored to bioSBM. This algorithm estimates the latent parameters that best explain the observed Hi-C interaction data, integrating both chromatin interaction frequencies and biochemical covariates.

Our approach is based on variational inference, a method well-suited for complex probabilistic models like the bioSBM, where exact inference is intractable. We optimize a variational lower bound on the model evidence, commonly referred to as the Evidence Lower Bound (ELBO), which enables us to approximate the posterior distribution of the latent variables.

The variational inference procedure optimizes the ELBO, defined as:

$$\mathcal{L}(q, \Psi) = \mathbb{E}_q [\log P(Y, \eta_{1:N}, Z|\Psi, X) - \log q(\eta_{1:N}, Z)] \quad (5)$$

where Y and X are for the OE Hi-C interaction data and the biochemical covariates respectively, $\eta_{1:N}$ are the latent membership vectors ($\theta_{1:N}$ are the normalized versions), Z represents the community assignments for edges, Ψ includes the global model parameters, and $\mathbb{E}_q[\cdot]$ denotes the expectation value with respect to the variational distribution q . The variational distribution $q(\eta_{1:N}, Z)$ approximates the true posterior distribution $P(\eta_{1:N}, Z|Y, X, \Psi)$.

The algorithm proceeds in two main steps:

1. **Variational E-step:** We update the variational distributions of the latent variables, η_i and z_{ij} , by maximizing the ELBO with respect to the variational parameters. The factorized variational distributions take the form:

$$q(\eta_i) \propto \exp \left\{ \log P(\eta_i|\mu_i, \Sigma) + \mathbb{E}_{q(Z)} [\log P(Z|\eta_i)] \right\} \quad (6)$$

$$q(z_{ij}) \propto \exp \left\{ \mathbb{E}_{q(z_{ji})} [\log P(Y_{ij}|z_{ij}, z_{ji}, B)] + \mathbb{E}_{q(\eta_i)} [\log P(z_{ij}|\eta_i)] \right\} \quad (7)$$

Here, η_i are the continuous latent membership vectors, and z_{ij} are the discrete community assignments for edges.

2. **Variational M-step:** This step involves optimizing the model parameters $\Psi \equiv (\Sigma, \Gamma, B, \sigma^2)$ with the current estimates of the variational distributions. The matrix Γ maps the biochemical covariates to the latent space, while Σ is the covariance matrix capturing the variability in the latent memberships. The matrices B and σ^2 describe the mean interaction strengths and variances between communities.

The iterative process of alternating between the E-step and the M-step continues until convergence, at which

point the model parameters and variational distributions jointly provide an interpretation of the chromatin interaction patterns. For the detailed mathematical derivations and specific parameter update rules, refer to Sec. S1 in SM.

III. RESULTS

To train the model, we perform posterior inference using M pairs of biochemical covariates and Hi-C matrices $(X^\mu, Y^\mu)_{\mu=1}^M$, computing approximate posterior distributions over per-node latent membership vectors θ_i and the model parameters. In particular, the two sets of chromosomes we use are the odd-numbered chromosomes from 11 to 21 and the even-numbered chromosomes from 12 to 22. We use the model trained on one set to make predictions on the other and vice-versa. We applied the inference algorithm to data from the GM12878 lymphoblastoid cell line at a resolution of 100 kbps, and through Bayesian model selection, using evidence lower bound (ELBO) as a criterion, we determined that the optimal number of communities for our model is $K = 12$. This suggests a more complex organization structure that extends beyond the conventional binary A/B compartmentalization and the more nuanced subdivision in subcompartments (up to six) [9]. At the same time, our model provides a more concise representation of chromatin contacts than the 30 epigenetically distinct “*binding domains*” suggested by Esposito et al [42] using polymer modeling.

The *maximum-a-posteriori* (MAP) estimates of the vectors θ_i provide the most plausible community membership proportions for each node, based on the observation of experimental Hi-C maps and associated biochemical covariates. Along with the θ_i values, the inference process also estimates the global parameters that characterize the generative model. A key parameter is the matrix Γ (Sec. II C), which represents the linear transformation mapping biochemical features to the probabilities of belonging to each community, offering insights into how biochemical factors shape chromatin structure. Additionally, the matrix B encodes the interaction strengths between all pairs of communities.

A. bioSBM explains the hierarchical organization of the chromatin in terms of epigenomic marks

To evaluate the biological relevance of the communities identified by our model, we performed k -means clustering on the MAP membership vectors θ_i . Clustering into two groups allowed us to compare these clusters to known A/B compartments, while varying the number of clusters, depending on the number of significantly present subcompartments in each chromosome, enabled comparisons with the subcompartments defined by Rao et al. [9].

The results of the clustering showed a significant overlap with known biological annotations. Fig. 2 illustrates this comparison for chromosomes 16 and 19. Both the binary subdivision in A/B compartments and the more granular classification in subcompartments can be captured from the full mixed membership vectors inferred by our model. Further validation of the inferred communities was performed by assessing the enrichment of each k -means-derived cluster in the biochemical features x_i . These enrichments were compared to those observed in A/B compartments and subcompartments annotations (see Fig. 3), where we can see a near-perfect agreement of bioSBM results with the enrichment of the binary A/B classification and a very good agreement with the enrichment of the subcompartments defined by [9].

We extended this analysis to other chromosomes (see Sec. S2 and Table S1 in SM for details on datasets used) and computed the similarity between the subdivision found by clustering the membership vectors and those based on the biological annotations using the normalized mutual information (NMI) score. We obtained a median NMI score (which ranges from 0 to 1) of $\text{NMI}^{\text{A/B}} \simeq 0.79$ for the binary clustering, and $\text{NMI}^{\text{subcomp}} \simeq 0.49$ for the subcompartments. These results suggest that while our model’s communities largely align with known biological structures, the correspondence is incomplete. The partial agreement with subcompartments suggests that our model may capture additional layers of chromatin interaction complexity that may be missed by conventional classification methods.

Importantly, the model goes beyond merely segmenting chromatin regions based on their epigenetic features; it also illustrates how these different classes interact, as represented by the matrix B , where each entry B_{kg} encodes the interaction strength between class k and g . Fig. 4(a) shows that each of the 12 inferred communities strongly correlates with distinct epigenetic marks. Interestingly, despite the apparent redundancy for some of the communities at the level of epigenomic profiles, there are clear distinctions between the interaction patterns of different classes. For instance (see Fig. 4(b)), classes 0 and 2 have similar epigenetic profiles but regions predominantly associated with class 0 have reduced contact frequency with regions primarily linked to class 2, and vice versa. Another notable observation is that classes 4 and 5 share a similar enrichment profile but differ in interaction patterns. Class 4 interacts only with itself and the epigenetically similar class 5, while class 5 interacts positively with classes 6, 7, and 8 as well. The inset of Fig. 4(c) shows that regions with non-zero probabilities of belonging to classes 4 and 5 overlap with clusters corresponding to the B2 and B4 compartments. Here however nodes need not be categorized into one class or another, they can share properties of multiple communities in different proportions.

Altogether these observations show that the bioSBM representation of chromatin interaction patterns provides a more nuanced description than the one provided by

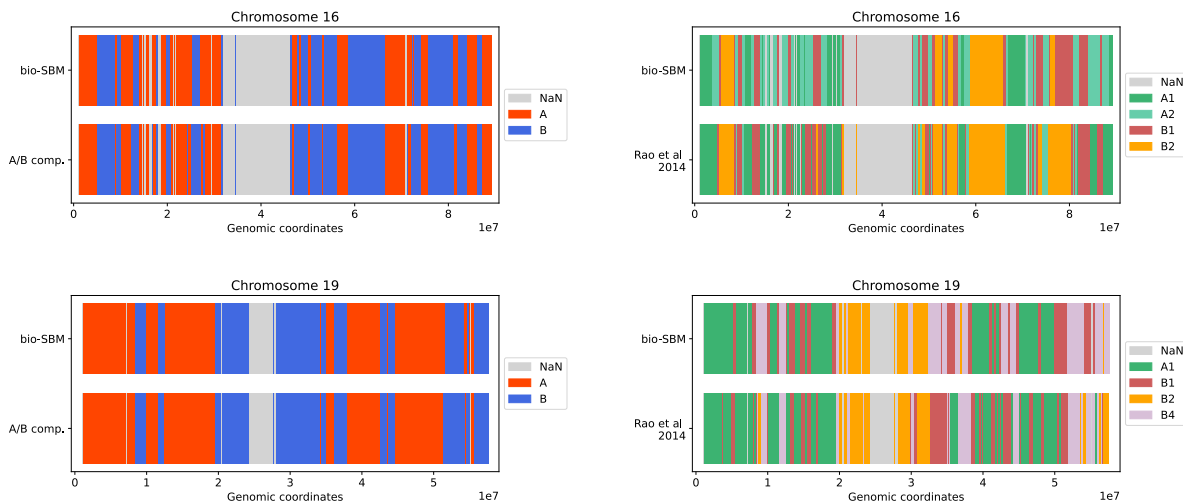


FIG. 2. The latent representation found through inference of the bioSBM model is biologically meaningful. The top row in each plot represents the clusters obtained by applying k -means on the MAP membership vectors inferred through our algorithm. The bottom rows are biological annotations.

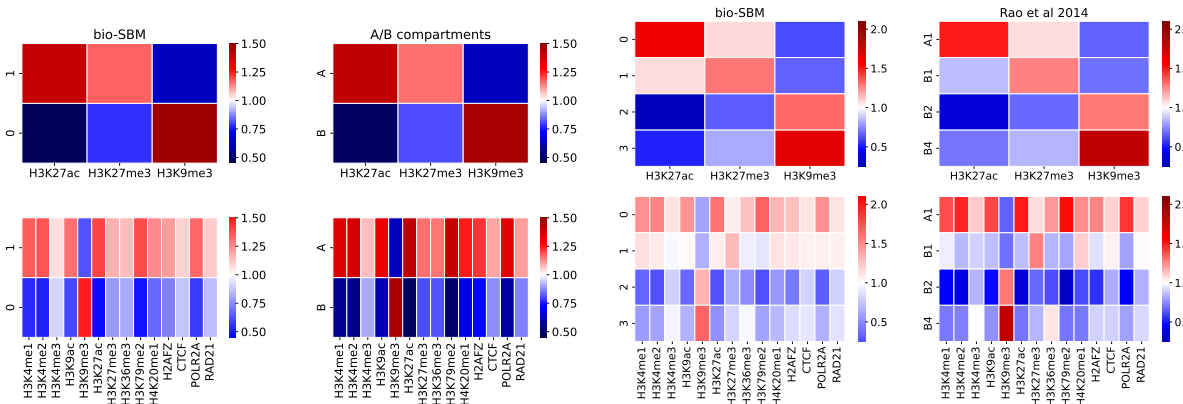


FIG. 3. Log fold enrichment in biochemical features (such as the presence of histone marks) for chromosome 19. The patterns of enrichment for our clusters are in good agreement with the enrichment found for A/B compartments and subcompartments.

simple segmentation of the genome in different clusters.

B. bioSBM predicts the structure of the chromatin in unseen cell lines

The previous section focussed on an analysis of the interpretability of bioSBM, showing that the inferred model parameters recapitulate and extend previous observations on the epigenetic state of the chromatin and its compartments. In this Section, we leverage the generative structure of bioSBM to test whether the simple representation of the genome contacts in terms of interactions between a limited number of communities and the fact that these communities can be determined starting from independent measurements of biochemical covariates is enough to reproduce long-range genome-wide chromatin contact patterns.

Specifically, given matrices B and Γ , inferred from some training chromosomes in some conditions, and biochemical measurements for test chromosomes (either different chromosomes in the same cell line, or chromosomes from a different cell line), we can compute their community structure as $\theta_i = \Gamma x_i$. With the predicted community structure, we use the matrix B to sample contact maps and compute their expectations, which can then be compared to experimentally obtained Hi-C maps (refer to Sec. S3 in SM for technical details).

Fig. 5 illustrates the testing pipeline, providing an example of the predicted Hi-C map and predicted Pearson correlation matrix for chromosome 19. Here, biochemical covariates associated with chromosome 19 were used, while the block model interaction parameters were inferred from a different set of chromosomes. The strong correlation between experimental and predicted maps, as quantified by Pearson correlation coefficients (Fig. 6),

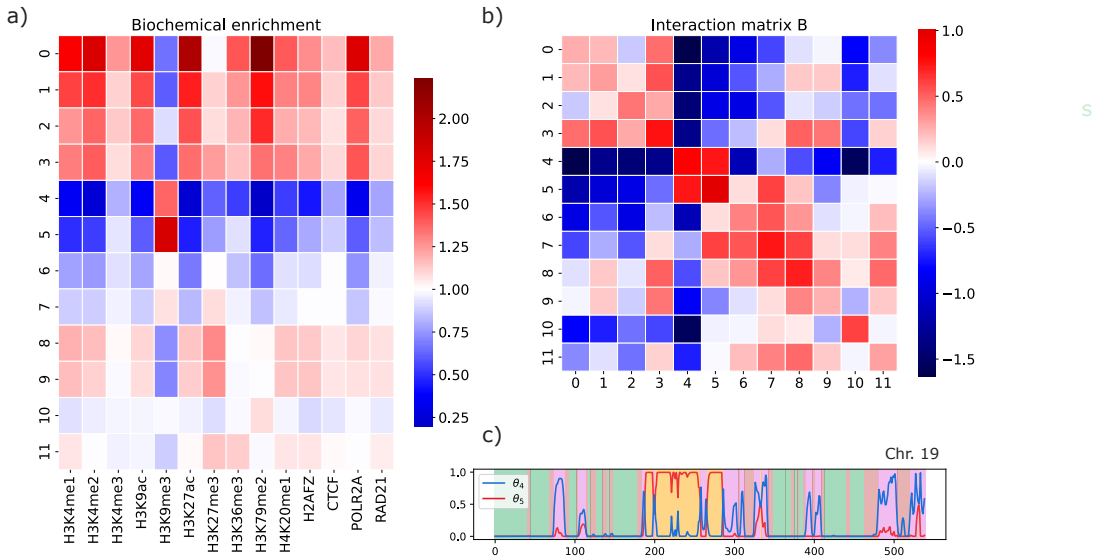


FIG. 4. (a) Enrichment of mixed membership communities in the biochemical features used in the model. Each community correlates with distinct epigenetic features. (b) Interaction intensities between all pairs of communities. (c) Membership proportions of communities 4 and 5 as a function of node indices.

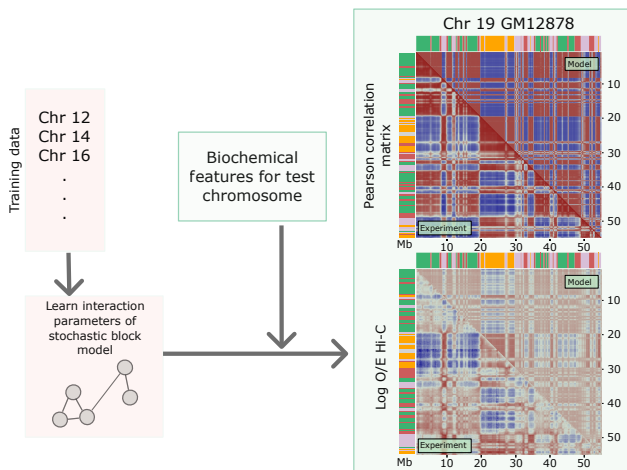


FIG. 5. The figure shows the Hi-C maps and the Pearson correlation matrix for chromosome 19. These maps are computed with the biochemical covariates associated with the chromosome and the parameters for the stochastic block model learned on a different set of chromosomes. The bottom triangle of each map is the experimentally observed Hi-C or Pearson correlation matrix, the top triangles are the model-generated counterparts. Above each map the colored bars represent the segmentation of the genome arising from k-mean clustering of the model mixed-membership vectors, while the bars on the left of each map are the subcompartment annotations from [9]

demonstrates the model’s predictive accuracy. Interestingly, the difference in accuracy between the training and test sets was marginal, with a one-tailed Mann-Whitney U test yielding a p-value of 0.12. Therefore, bioSBM effectively generalizes across different chromosomes within

the same cell line, suggesting that the inferred associations B_{kg} between communities and the biochemistry-to-structure map Γ reflect genuine chromatin interactions.

Further support for this conclusion comes from a comparison with state-of-the-art results reported by Esposito et al (2022) [42], where a code linking 1D chromatin marks to the interaction parameters of a polymer model was learned. While the polymer model similarly recapitulates chromatin contact patterns in training data, testing on unseen chromosomes from the GM12878 cell line strongly favors the bioSBM model in terms of predictive performance (see Fig. 6).

Finally, we tested the model on data from the human colorectal carcinoma cell line HCT116, where auxin-inducible degron (AID) technology was used to degrade RAD21 [43]. We apply the model as trained on GM12878 to independent covariates from the ENCODE Project [44] obtained from experiments on the HCT116 cell line without AID-induced RAD21 degradation. In this case, we observe a decrease in predictive accuracy, likely due to the mismatch between the learned map Γ , which includes RAD21, and a biological sample where the latter has been degraded. Additionally, RAD21 deletion could have induced slight changes also in the other covariates, further affecting predictive performance. Notably, when the RAD21 covariate was excluded from the model (by setting the corresponding row in the feature matrix X to zero), performance improved significantly (p -value = 0.03), suggesting the flexibility and robustness of bioSBM in capturing chromatin interactions under different cellular conditions.

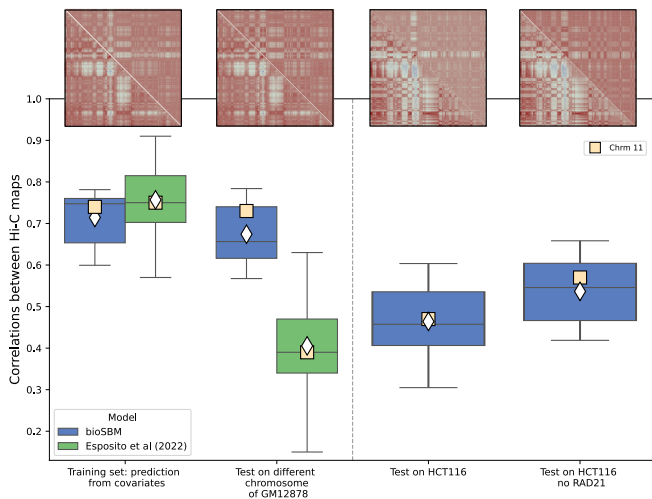


FIG. 6. Box plots of correlations between experimental maps and model generated maps, where the individual data points are single chromosomes. White diamonds represent the means of the box plots and the ivory squares are the correlation values for the example chromosome 11. The insets show comparisons of experimental maps (lower triangular part) and model-generated maps (upper triangle). To test whether the training performance was significantly higher or not than the test on different chromosomes on the same cell line we performed a one-tailed Mann-Whitney U test, that yielded a negative answer (p -value = 0.12). For tests on HCT116 we see that the correlations are higher in the RAD21 depleted scenario (tested for significance with a p -value = 0.03). The green box plots refer to correlations reported from Esposito *et al.* (2022) [42] for a polymer-based model on the same dataset.

IV. DISCUSSION AND CONCLUSIONS

The bioSBM model introduced in this study offers a novel approach for modeling long-range chromatin interactions by integrating Hi-C data with biochemical covariates such as histone modifications and binding of transcription factors. By employing a mixed membership stochastic block model, we capture a more refined and nuanced view of chromatin structure, extending beyond the traditional binary A/B and sub-compartments framework. Our results show that the 12 communities identified by bioSBM correlate with known epigenetic features, reinforcing the idea that chromatin interactions are closely tied to the biochemical landscape of the genome. The partial agreement with subcompartments suggests that our model may capture additional layers of chromatin interaction complexity that may be missed by conventional classification methods.

Although more abstract than polymer models, which explicitly take into account (to varying degrees of detail) the physical nature of the linear chromosomes, the latent representation learned by bioSBM remains biologically interpretable. The inferred associations between biochemistry and structure encoded in the linear map Γ

and the communities interactions contained in B provide a starting point for systematically exploring more mechanistic descriptions of how chromatin folding is affected by nuclear biochemical processes.

The predictive power of the model is another important contribution. By leveraging biochemical covariates, bioSBM can accurately predict chromatin contacts across different chromosomes and cell lines, comparing favorably with state-of-the-art polymer approaches [42]. Notably, the model’s robustness is highlighted by its performance on the HCT116 cell line, where the removal of the RAD21 covariate improved predictive accuracy, indicating that bioSBM can adapt to different chromatin environments and capture interactions under varying conditions, such as RAD21 depletion. Interestingly, bioSBM also compares favorably with recent deep-learning models. Many deep learning approaches predict Hi-C maps using only DNA sequence data as input features [14, 15], which limits their ability to capture cell-type specific variations. In contrast, bioSBM explicitly incorporates epigenetic features, making it more suited for cell-type-specific predictions. Additionally, bioSBM’s predictive power is comparable to a recent deep learning model that does include epigenetic signals [17]. However, deep learning models have a distinct advantage in terms of computational power, allowing them to predict Hi-C maps at higher resolutions and model small-scale perturbations, such as the effects of single nucleotide polymorphisms (SNPs) [14]. While our model cannot operate at this fine-grained scale, it remains effective in predicting the effects of larger-scale manipulations such as the AID-induced RAD21 reported above. Crucially, bioSBM stands out for its interpretability: every parameter has a clear probabilistic semantic, allowing their analysis to uncover a clear biological meaning. This makes bioSBM a valuable, flexible tool for studying chromatin organization in diverse cellular contexts.

While this study focuses on Hi-C data, the so-called enrichment methods [45], such as Promoter Capture Hi-C (PCHi-C) [46] or ChIA-PET [47, 48], may offer more functionally relevant perspectives on chromatin structure. PCHi-C, for example, highlights promoter regions interactions, while ChIA-PET focuses on interactions involving specific proteins. These methods present challenges for polymer models because they capture interactions between non-contiguous regions. However, bioSBM, being graph-based, could accommodate these non-contiguous interactions with some adaptation. Though some graph-based studies exist that link nuclear biochemistry to chromatin structure as assayed by these enrichment-based data [21, 22], a fully generative predictive model mapping biochemistry to the chromatin interaction patterns, such as that provided by bioSBM for Hi-C, has yet to be developed. With appropriate adjustments, bioSBM could readily be extended to accommodate these data types.

In conclusion, the bioSBM model successfully balances interpretability and scalability, offering a valuable tool for

understanding the relationship between chromatin structure and its biochemical underpinnings. By incorporating biochemical features and allowing for mixed memberships, bioSBM provides a more flexible and biologically meaningful representation of chromatin interac-

tions. The model's predictive power and adaptability across different cellular contexts underscore its potential for further applications, such as exploring chromatin dynamics in different developmental stages or disease states.

-
- [1] A. G. Matera, M. Izaguirre-Sierra, K. Praveen, and T. K. Rajendra, Nuclear Bodies: Random Aggregates of Sticky Proteins or Crucibles of Macromolecular Assembly?, *Developmental Cell* **17**, 639 (2009).
- [2] S. F. Banani, H. O. Lee, A. A. Hyman, and M. K. Rosen, Biomolecular condensates: organizers of cellular biochemistry, *Nature Reviews Molecular Cell Biology* **18**, 285 (2017), publisher: Nature Publishing Group.
- [3] L. Wang, Y. Gao, X. Zheng, C. Liu, S. Dong, R. Li, G. Zhang, Y. Wei, H. Qu, Y. Li, C. D. Allis, G. Li, H. Li, and P. Li, Histone Modifications Regulate Chromatin Compartmentalization by Contributing to a Phase Separation Mechanism, *Molecular Cell* **76**, 646 (2019).
- [4] A.-M. Ladouceur, B. S. Parmar, S. Biedzinski, J. Wall, S. G. Tope, D. Cohn, A. Kim, N. Soubry, R. Reyes-Lamothe, and S. C. Weber, Clusters of bacterial RNA polymerase are biomolecular condensates that assemble through liquid-liquid phase separation, *Proceedings of the National Academy of Sciences* **117**, 18540 (2020), publisher: Proceedings of the National Academy of Sciences.
- [5] J. Dekker, K. Rippe, M. Dekker, and N. Kleckner, Capturing Chromosome Conformation, *Science* **295**, 1306 (2002), number: 5558 Publisher: American Association for the Advancement of Science.
- [6] E. Lieberman-Aiden, N. L. van Berkum, L. Williams, M. Imakaev, T. Ragozcy, A. Telling, I. Amit, B. R. Lajoie, P. J. Sabo, M. O. Dorschner, R. Sandstrom, B. Bernstein, M. A. Bender, M. Groudine, A. Gnirke, J. Stamatoyannopoulos, L. A. Mirny, E. S. Lander, and J. Dekker, Comprehensive mapping of long range interactions reveals folding principles of the human genome, *Science (New York, N.Y.)* **326**, 289 (2009), number: 5950.
- [7] M. H. Nichols and V. G. Corces, Principles of 3D compartmentalization of the human genome, *Cell Reports* **35**, 109330 (2021).
- [8] M. J. Rowley and V. G. Corces, Organizational principles of 3D genome architecture, *Nature Reviews Genetics* **19**, 789 (2018), number: 12 Publisher: Nature Publishing Group.
- [9] S. S. P. Rao, M. H. Huntley, N. C. Durand, E. K. Stamenova, I. D. Bochkov, J. T. Robinson, A. L. Sanborn, I. Machol, A. D. Omer, E. S. Lander, and E. L. Aiden, A 3D Map of the Human Genome at Kilobase Resolution Reveals Principles of Chromatin Looping, *Cell* **159**, 1665 (2014), publisher: Elsevier.
- [10] S. Bianco, D. G. Lupiáñez, A. M. Chiariello, C. Annunziatella, K. Kraft, R. Schöpflin, L. Wittler, G. Andrey, M. Vingron, A. Pombo, S. Mundlos, and M. Nicodemi, Polymer physics predicts the effects of structural variants on chromatin architecture, *Nature Genetics* **50**, 662 (2018), number: 5 Publisher: Nature Publishing Group.
- [11] M. Di Pierro, R. R. Cheng, E. Lieberman Aiden, P. G. Wolynes, and J. N. Onuchic, De novo prediction of human chromosome structures: Epigenetic marking patterns encode genome architecture, *Proceedings of the National Academy of Sciences* **114**, 12126 (2017), number: 46 Publisher: Proceedings of the National Academy of Sciences.
- [12] D. Jost, P. Carrivain, G. Cavalli, and C. Vaillant, Modeling epigenome folding: formation and dynamics of topologically associated chromatin domains, *Nucleic Acids Research* **42**, 9553 (2014).
- [13] A. C. Y. Zhang, A. Rosa, and G. Sanguinetti, Bottom-up data integration in polymer models of chromatin organization, *Biophysical Journal* **123**, 184 (2024).
- [14] G. Fudenberg, D. R. Kelley, and K. S. Pollard, Predicting 3D genome folding from DNA sequence with Akita, *Nature Methods* **17**, 1111 (2020), number: 11 Publisher: Nature Publishing Group.
- [15] R. Schwessinger, M. Gosden, D. Downes, R. C. Brown, A. M. Oudelaar, J. Telenius, Y. W. Teh, G. Lunter, and J. R. Hughes, DeepC: predicting 3D genome folding using megabase-scale transfer learning, *Nature Methods* **17**, 1118 (2020), publisher: Nature Publishing Group.
- [16] J. Zhou, Sequence-based modeling of three-dimensional genome architecture from kilobase to chromosome scale, *Nature Genetics* **54**, 725 (2022), publisher: Nature Publishing Group.
- [17] R. Yang, A. Das, V. R. Gao, A. Karbalayghareh, W. S. Noble, J. A. Bilmes, and C. S. Leslie, Epiphany: predicting Hi-C contact maps from 1D epigenomic signals, *Genome Biology* **24**, 134 (2023).
- [18] M. E. J. Newman, *Networks: an introduction*, reprinted ed. (Oxford University Press, Oxford, 2016).
- [19] I. Cabrerós, E. Abbe, and A. Tsigirós, Detecting Community Structures in Hi-C Genomic Data (2015), arXiv:1509.05121 [cs, q-bio, stat].
- [20] H. K. Norton, D. J. Emerson, H. Huang, J. Kim, K. R. Titus, S. Gu, D. S. Bassett, and J. E. Phillips-Cremins, Detecting hierarchical genome folding with network modularity, *Nature Methods* **15**, 119 (2018), number: 2 Publisher: Nature Publishing Group.
- [21] V. Pancaldi, E. Carrillo-de Santa-Pau, B. M. Javierre, D. Juan, P. Fraser, M. Spivakov, A. Valencia, and D. Rico, Integrating epigenomic data and 3D genomic structure with a new measure of chromatin assortativity, *Genome Biology* **17**, 152 (2016), number: 1.
- [22] V. Pancaldi, Chromatin Network Analyses: Towards Structure-Function Relationships in Epigenomics, *Frontiers in Bioinformatics* **1**, 10.3389/fbinf.2021.742216 (2021), publisher: Frontiers.
- [23] V. Pancaldi, Network models of chromatin structure, *Current Opinion in Genetics & Development* **80**, 102051 (2023).
- [24] Y. J. Wang and G. Y. Wong, Stochastic Blockmodels for Directed Graphs, *Journal of the American Statistical Association* **82**, 8 (1987).

- [25] T. A. Snijders and K. Nowicki, Estimation and Prediction for Stochastic Blockmodels for Graphs with Latent Block Structure, *Journal of Classification* **14**, 75 (1997), number: 1.
- [26] A. Frieze and M. Karoński, *Introduction to Random Graphs* (Cambridge University Press, Cambridge, 2015).
- [27] B. Bollobás, *Random Graphs*, 2nd ed., Cambridge Studies in Advanced Mathematics (Cambridge University Press, Cambridge, 2001).
- [28] C. Lee and D. J. Wilkinson, A review of stochastic block models and extensions for graph clustering, *Applied Network Science* **4**, 1 (2019), number: 1 Publisher: SpringerOpen.
- [29] J.-J. Daudin, F. Picard, and S. Robin, A mixture model for random graphs, *Statistics and Computing* **18**, 173 (2008).
- [30] E. Abbe, Community Detection and Stochastic Block Models: Recent Developments, *Journal of Machine Learning Research* **18**, 1 (2018).
- [31] J. W. Whitaker, Z. Chen, and W. Wang, Predicting the human epigenome from DNA motifs, *Nature Methods* **12**, 265 (2015), number: 3 Publisher: Nature Publishing Group.
- [32] A. Rosa, N. B. Becker, and R. Everaers, Looping Probabilities in Model Interphase Chromosomes, *Biophysical Journal* **98**, 2410 (2010), number: 11.
- [33] A. Y. Grosberg, How two meters of DNA fit into a cell nucleus: Polymer models with topological constraints and experimental data, *Polymer Science Series C* **54**, 1 (2012).
- [34] J. D. Halverson, J. Smrek, K. Kremer, and A. Y. Grosberg, From a melt of rings to chromosome territories: the role of topological constraints in genome folding, *Reports on Progress in Physics. Physical Society (Great Britain)* **77**, 022601 (2014), number: 2.
- [35] D. S. Johnson, A. Mortazavi, R. M. Myers, and B. Wold, Genome-Wide Mapping of in Vivo Protein-DNA Interactions, *Science* **316**, 1497 (2007), number: 5830 Publisher: American Association for the Advancement of Science.
- [36] G. M. Allenby, P. E. Rossi, and R. E. McCulloch, *Hierarchical Bayes Models: A Practitioners Guide* (2005).
- [37] A. Gelman, J. B. Carlin, H. S. Stern, D. B. Dunson, A. Vehtari, and D. B. Rubin, *Bayesian data analysis*, third edition ed., Texts in statistical science series (CRC Press, Taylor and Francis Group, Boca Raton London New York, 2014).
- [38] M. Mariadassou, S. Robin, and C. Vacher, Uncovering latent structure in valued graphs: A variational approach, *The Annals of Applied Statistics* **4**, 715 (2010), publisher: Institute of Mathematical Statistics.
- [39] E. M. Airolidi, D. M. Blei, S. E. Fienberg, and E. P. Xing, Mixed Membership Stochastic Blockmodels, *Journal of machine learning research : JMLR* **9**, 1981 (2008).
- [40] J. Aitchison, The Statistical Analysis of Compositional Data, *Journal of the Royal Statistical Society: Series B (Methodological)* **44**, 139 (1982).
- [41] D. M. Blei and J. D. Lafferty, A correlated topic model of Science, *The Annals of Applied Statistics* **1**, 10.1214/07-AOAS114 (2007), arXiv:0708.3601 [stat].
- [42] A. Esposito, S. Bianco, A. M. Chiariello, A. Abraham, L. Fiorillo, M. Conte, R. Campanile, and M. Nicodemi, Polymer physics reveals a combinatorial code linking 3D chromatin architecture to 1D chromatin states, *Cell Reports* **38**, 110601 (2022).
- [43] S. S. P. Rao, S.-C. Huang, B. Glenn St Hilaire, J. M. Engreitz, E. M. Perez, K.-R. Kieffer-Kwon, A. L. Sanborn, S. E. Johnstone, G. D. Bascom, I. D. Bochkov, X. Huang, M. S. Shamim, J. Shin, D. Turner, Z. Ye, A. D. Omer, J. T. Robinson, T. Schlick, B. E. Bernstein, R. Casellas, E. S. Lander, and E. L. Aiden, Cohesin Loss Eliminates All Loop Domains, *Cell* **171**, 305 (2017).
- [44] ENCODE (2024).
- [45] I. Jerkovic´ and G. Cavalli, Understanding 3D genome organization by multidisciplinary methods, *Nature Reviews Molecular Cell Biology* **22**, 511 (2021), number: 8 Publisher: Nature Publishing Group.
- [46] S. Schoenfelder, B.-M. Javierre, M. Furlan-Magaril, S. W. Wingett, and P. Fraser, Promoter Capture Hi-C: High-resolution, Genome-wide Profiling of Promoter Interactions, *Journal of Visualized Experiments : JoVE* , 57320 (2018).
- [47] G. Li, M. J. Fullwood, H. Xu, F. H. Mulawadi, S. Velkov, V. Vega, P. N. Ariyaratne, Y. B. Mohamed, H.-S. Ooi, C. Tennakoon, C.-L. Wei, Y. Ruan, and W.-K. Sung, ChIA-PET tool for comprehensive chromatin interaction analysis with paired-end tag sequencing, *Genome Biology* **11**, R22 (2010).
- [48] G. Li, L. Cai, H. Chang, P. Hong, Q. Zhou, E. V. Kulakova, N. A. Kolchanov, and Y. Ruan, Chromatin Interaction Analysis with Paired-End Tag (ChIA-PET) sequencing technology and application, *BMC Genomics* **15**, S11 (2014).
- [49] C. Wang and D. M. Blei, Variational Inference in Nonconjugate Models (2013), issue: arXiv:1209.4360 arXiv:1209.4360 [stat].
- [50] J. Nocedal and S. J. Wright, *Numerical Optimization*, Springer Series in Operations Research and Financial Engineering (Springer New York, 2006).
- [51] 4DN Data Portal (2024).
- [52] N. C. Durand, J. T. Robinson, M. S. Shamim, I. Machol, J. P. Mesirov, E. S. Lander, and E. L. Aiden, Juicebox Provides a Visualization System for Hi-C Contact Maps with Unlimited Zoom, *Cell Systems* **3**, 99 (2016).
- [53] `deeptools/pyBigWig` (2024), original-date: 2015-07-31T12:07:36Z.
-

Supplemental Material

bioSBM: a random graph model to integrate epigenomic data in chromatin structure prediction

Alex Chen Yi Zhang, Angelo Rosa, Guido Sanguinetti

CONTENTS

I.	Introduction	1
II.	Model and Methods	2
	A. SBM and its generalization	2
	B. bioSBM: a covariate dependent MMSBM for long-range chromatin contacts	2
	C. Posterior inference	4
III.	Results	5
	A. bioSBM explains the hierarchical organization of the chromatin in terms of epigenomic marks	5
	B. bioSBM predicts the structure of the chromatin in unseen cell lines	6
IV.	Discussion and conclusions	8
	References	9
S1.	Derivation of the Variational Bayes Expectation Maximization (VBEM) algorithm for bioSBM	S2
	A. Variational E-step	S2
	B. Variational M-step	S4
S2.	Dataset preprocessing	S5
S3.	Simulation of predicted maps	S5
	Supplemental Table and Figures	S6

S1. DERIVATION OF THE VARIATIONAL BAYES EXPECTATION MAXIMIZATION (VBEM) ALGORITHM FOR BIOSBM

In this Section, we provide a more detailed derivation of the equations at the core of the Variational Bayes Expectation Maximization (VBEM) algorithm for the model introduced in the paper. The quantities in our problem are:

- Observed data $Y \in \mathbb{R}^{N \times N}$: matrix representing Hi-C maps with a log-observed-over-expected normalization.
- Known node covariates $X \in \mathbb{R}^{P \times N}$: each row x_i is the P-dimensional feature vector associated to node i .
- Latent variables: $\theta_{i=1 \dots N}$ and z_{ij} and z_{ji} for $i = 1 \dots N$, $j = 1 \dots i - 1$, where θ_i is the latent membership vector for node i and z_{ji} is the membership assignment of node i in the interaction with node j .
- Hyperparameters: $(\Sigma, \Gamma, B, \sigma^2) \equiv \Psi$.

A lower bound for the evidence $P(Y|\Sigma, \Gamma, B, X)$ is given by the ELBO (literally *Evidence Lower BOund*):

$$\begin{aligned}
\mathcal{L}(q, \Psi) &= \mathbb{E}_q [\log P(Y, \eta_{1:N}, Z|\Psi, X) - \log q(\eta_{1:N}, Z)] = \\
&= \mathbb{E}_q [\log P(\eta_{1:N}|\Sigma, \Gamma, X) + \log P(Z|\eta_{1:N}) + \log P(Y|Z, B) - \log q(\eta_{1:N}, Z)] \\
&= \sum_{i=1}^N \mathbb{E}_q [\log P(\eta_i|\mu_i = \Gamma x_i, \Sigma)] + \sum_{i=1}^N \sum_{j=1}^{i-1} \mathbb{E}_q [\log P(z_{ij}|\theta_i)P(z_{ji}|\theta_j)] \\
&\quad + \sum_{i=1}^N \sum_{j=1}^{i-1} \mathbb{E}_q [\log P(Y_{ij}|z_{ij}, z_{ji}, B)] + H(q) \leq P(Y|\Psi, X)
\end{aligned} \tag{S1}$$

The inequality becomes an equality if the distribution $q(\eta_{1:N}, Z)$ is exactly the posterior distribution. The variational Bayes *Expectation-Maximization* (VBEM) method consists of iteratively tightening this bound to approximate the true posterior. In the E-step of the algorithm, one needs to maximize the ELBO with respect to the variational distribution $q(\eta_{1:N}, Z)$ while in the M-step one carries out the maximization with respect to the hyperparameters.

A. Variational E-step

To carry out the optimization task we take a mean-field assumption on the shape of the variational distribution $q(\eta, Z)$, where we assume the factorized form $q(\eta, Z) = q(\eta)q(Z) = \prod_i q(\eta_i) \prod_{i \neq j} q(z_{ij})$. By taking the functional derivatives of the ELBO with respect to the variational distribution and by fixing them to zero one finds the update equations for the E-step, which in the general form read:

$$q(\eta_i) \propto \exp \{ \log P(\eta_i|\mu_i, \Sigma) + \mathbb{E}_{q(Z)} [\log P(Z|\eta_i)] \} \tag{S2}$$

$$q(z_{ij}) \propto \exp \{ \mathbb{E}_{q(z_{ji})} [\log P(Y_{ij}|z_{ij}, z_{ji}, B)] + \mathbb{E}_{q(\eta_i)} [\log P(z_{ij}|\eta_i)] \} \tag{S3}$$

Because of the non-conjugacy of the logistic normal prior with the multinomial likelihood, we will resort to the approximation technique introduced by [49]. More explicitly:

$$q(\eta_i) \propto \exp \{ \log P(\eta_i|\mu_i, \Sigma) + \sum_{j(\neq i)} \mathbb{E}_{q(z_{ij})} [\log P(z_{ij}|\eta_i)] \} := \exp \{ f(\eta_i) \} \tag{S4}$$

Let $\hat{\eta}_i$ be the maximum a-posteriori value of the parameter. The method introduced by [49] consists in approximating the function $f(\eta_i)$ with its expansion up to second order around $\hat{\eta}_i$. This gives the following Gaussian approximation for the variational approximation $q(\eta_i)$:

$$q(\eta_i) \simeq \mathcal{N}(\eta_i | \hat{\eta}_i, -\nabla^2 f(\hat{\eta}_i)^{-1}) \tag{S5}$$

Therefore we need the function at the exponent to be doubly differentiable and to find the maximum a posterior (variational) estimate $\hat{\eta}_i$ we can use standard gradient ascent techniques. If we write out explicitly the function we have that

$$f(\eta_i) = -\frac{1}{2}(\eta_i - \mu_i)^T (\Sigma)^{-1} (\eta_i - \mu_i) + \sum_{j(\neq i)} \sum_{k=1}^K \left(\eta_{i,k} - \log \sum_{k'=1}^K \exp(\eta_{i,k'}) \right) \mathbb{E}_{q(z_{ij})} [z_{ij,k}] \tag{S6}$$

Defining $\theta(\eta)$ as the *softmax* of η i.e. $\theta(\eta)_k = \exp(\eta_k) / \sum_{k'} \exp(\eta_{k'})$ we can obtain the gradient and the Hessian matrix of $f(\eta_i)$.

$$\nabla f(\eta_i) = \sum_{j(\neq i)}^N \left(\mathbb{E}_{q(z_{ij})}[z_{ij}] - \theta(\eta_i) \sum_{k=1}^K \mathbb{E}_{q(z_{ij})}[z_{ij,k}] \right) - \Sigma^{-1}(\eta_i - \mu_i) \quad (\text{S7})$$

$$\nabla^2 f(\eta_i) = \sum_{j(\neq i)}^N \left((\text{diag}(\theta(\eta_i)) - \theta(\eta_i)\theta(\eta_i)^T) \sum_{k=1}^K \mathbb{E}_{q(z_{ij})}[z_{ij,k}] \right) - \Sigma^{-1} \quad (\text{S8})$$

For the topic assignments distributions we have $q(z_{ij}) = \text{Mult}(\phi_{ij})$ with ϕ_{ij} as variational parameters, then we can explicit the expectations in the above expressions as:

$$\nabla f(\eta_i) = -(N-1)\theta(\eta_i) + \sum_{j(\neq i)}^N \phi_{ij} - \Sigma^{-1}(\eta_i - \mu_i) \quad (\text{S9})$$

$$\nabla^2 f(\eta_i) = -(N-1)(\text{diag}(\theta(\eta_i)) - \theta(\eta_i)\theta(\eta_i)^T) - \Sigma^{-1} \quad (\text{S10})$$

Where $\text{diag}(\theta)$ is the diagonal matrix where the non-zero elements are the components of θ . It can be shown that $-\nabla^2 f(\eta_i)$ is always a positive definite matrix, therefore the method always gives a valid covariance matrix for the variational approximation. We use the Broyden–Fletcher–Goldfarb–Shanno (BFGS) algorithm with second-order backtracking line-search [50]. The optimization procedure returns $(\hat{\eta}_i, -\nabla^2 f(\hat{\eta}_i)^{-1})$, thereby updating the variational distribution on η , $q(\eta_i) \simeq \mathcal{N}(\eta_i | \hat{\eta}_i, -\nabla^2 f(\hat{\eta}_i)^{-1})$. This is the E-step for the membership distributions per node. This step, as for most variational mean field methods for mixed membership block models, has a cost which is $\sim \mathcal{O}(N^2)$.

For the topic assignments posteriors we explicitly write Eq. (S3) and we get that for every (i, j) and topic k

$$\begin{aligned} \phi_{ij,k} &\propto \exp \left\{ \sum_{g=1}^K \phi_{ji,g} \log P(Y_{ij} | B_{kg}, \sigma_{kg}) + \mathbb{E}_{q(\eta_i)}[\log P(z_{ij} | \eta_i)] \right\} \\ &= \exp \{ \mathbb{E}_{q(\eta_i)}[\log P(z_{ij} | \eta_i)] \} \prod_{g=1}^K P(Y_{ij} | B_{kg}, \sigma_{kg})^{\phi_{ji,g}} \end{aligned} \quad (\text{S11})$$

The term in the exponent reads:

$$\begin{aligned} \mathbb{E}_{q(\eta_i)}[\log P(z_{ij} | \eta_i)] &= \mathbb{E}_{q(\eta_i)}[\eta_{i,k} - \log \sum_{g=1}^K \exp(\eta_{i,g})] \\ &= \lambda_{i,k} - \int d\eta_i \mathcal{N}(\lambda_i, \nu_i) \log \sum_{g=1}^K \exp(\eta_{i,g}) \end{aligned} \quad (\text{S12})$$

By imposing normalization $\sum_k \phi_{ij,k} = 1$ for all pairs (i, j) the updates for the topic assignments posteriors become

$$\phi_{ij,k} \propto \exp(\lambda_{i,k}) \prod_{g=1}^K P(Y_{ij} | B_{kg} \sigma_{kg})^{\phi_{ji,g}} \quad (\text{S13})$$

Now, if we substitute in the Gaussian edge likelihood, we get the explicit update equations:

$$\log \phi_{ij,k} = \lambda_{i,k} - \sum_{g=1}^K \left[\frac{(Y_{ij} - B_{kg})^2}{2\sigma_{kg}} + \frac{\log \sigma_{kg}}{2} \right] \phi_{ji,g} + \text{const.} \quad (\text{S14})$$

Everything described until now represents the E-step of the VBEM algorithm and the updates are performed with fixed $(\Sigma, \Gamma, B, \sigma)$. The values for these parameters are updated in the M-step where instead we fix the variational parameters $\{\lambda_i, \nu_i\}$ for $i = 1 \dots N$ and ϕ_{ij} for $i \neq j$ that are optimized in the E-step.

B. Variational M-step

For the global covariance matrix, we need to take the matrix derivative of the terms in the ELBO that contain Σ . By exploiting some properties of matrix derivatives we find that:

$$\begin{aligned}
\frac{\partial \mathcal{L}(q, \Psi)}{\partial \Sigma^{-1}} &= \frac{1}{2} \frac{\partial}{\partial \Sigma^{-1}} \sum_{i=1}^N \mathbb{E}_{q(\eta_i)} [(\eta_i - \mu_i)^T (\Sigma)^{-1} (\eta_i - \mu_i) + \log |\Sigma^{-1}|] = \\
&= \frac{1}{2} \frac{\partial}{\partial \Sigma^{-1}} \sum_{i=1}^N \log |\Sigma^{-1}| - (\lambda_i - \mu_i)^T \Sigma^{-1} (\lambda_i - \mu_i) + \text{Tr}(\Sigma^{-1} \nu_i) = \\
&= \frac{N}{2} \Sigma^T - \frac{1}{2} \sum_{i=1}^N \nu_i^T + (\lambda_i - \mu_i)(\lambda_i - \mu_i)^T = 0
\end{aligned} \tag{S15}$$

Then the covariance matrix that maximizes the ELBO is given by

$$\hat{\Sigma} = \frac{1}{N} \sum_{i=1}^N \nu_i^T + (\lambda_i - \Gamma(x_i))(\lambda_i - \Gamma(x_i))^T \tag{S16}$$

Something additional that we can do is to add a regularization to the norm of Σ for numerical stability. In particular, something simple we can do is to regularize using the *nuclear norm*. For a generic matrix, the nuclear norm is given by the sum of the singular values; for a positive definite matrix such as Σ it is easy to show that the norm corresponds to the trace of the matrix $\text{Tr}(\Sigma)$. We then introduce an additional term $-R \cdot \text{Tr}(\Sigma)$ in the ELBO where $R = rN$ (selected with cross-validation) is the regularization strength and we write the explicit N dependence in such a way that all the terms of the ELBO containing Σ are *extensive*. The results analyzed in the paper are obtained using $r = 0.1$. With the additional term, Eq. S16 reads:

$$\begin{aligned}
\frac{N}{2} \Sigma - \frac{1}{2} \sum_{i=1}^N \nu_i^T + (\lambda_i - \mu_i)(\lambda_i - \mu_i)^T - R \frac{\partial \text{Tr}(\Sigma)}{\partial \Sigma^{-1}} &= \\
= \frac{N}{2} \Sigma - \frac{1}{2} \sum_{i=1}^N \nu_i^T + (\lambda_i - \mu_i)(\lambda_i - \mu_i)^T + R \Sigma^2 &= 0
\end{aligned} \tag{S17}$$

This equation is solved by the following matrix:

$$\hat{\Sigma} = \frac{1}{4r} \left[-\mathbb{I} + \sqrt{\mathbb{I} + \frac{8r}{N} \sum_{i=1}^N \nu_i^T + (\lambda_i - \Gamma(x_i))(\lambda_i - \Gamma(x_i))^T} \right] \tag{S18}$$

Which is the M-step update concerning the covariance matrix Σ .

The maximization of the ELBO with respect to B_{kg} and σ_{kg} entails:

$$\frac{\partial \mathcal{L}(q, \Psi)}{\partial B_{kg}} = \sum_{i \neq j} \phi_{ij,k} \phi_{ji,g} \frac{Y_{ij} - B_{kg}}{\sigma_{kg}} \tag{S19}$$

$$\frac{\partial \mathcal{L}(q, \Psi)}{\partial \sigma_{kg}} = \sum_{i \neq j} \phi_{ij,k} \phi_{ji,g} \left[\frac{(Y_{ij} - B_{kg})^2}{2\sigma_{kg}^2} - \frac{1}{2\sigma_{kg}} \right] \tag{S20}$$

By setting the above derivatives to zero we obtain:

$$\hat{B}_{kg} = \frac{\sum_{i \neq j} \phi_{ij,k} \phi_{ji,g} Y_{ij}}{\sum_{i \neq j} \phi_{ij,k} \phi_{ji,g}} \tag{S21}$$

$$\hat{\sigma}_{kg} = \frac{\sum_{i \neq j}^N \phi_{ij,k} \phi_{ji,g} (Y_{ij} - B_{kg})^2}{\sum_{i \neq j}^N \phi_{ij,k} \phi_{ji,g}} \quad (\text{S22})$$

These are the last update equations needed to specify the full VBEM algorithm for bioSBM.

Following these calculations, the explicit expression for the ELBO that we compute to monitor the progression of the optimization reads:

$$\begin{aligned} \mathcal{L} = & \frac{N}{2} \log |\Sigma^{-1}| - \frac{1}{2} \sum_{i=1}^N [(\lambda_i - \mu_i)^T \Sigma^{-1} (\lambda_i - \mu_i) + \text{Tr}(\Sigma^{-1} \nu_i)] + \sum_{i \neq j}^N \sum_{k=1}^K \phi_{ij,k} \lambda_{i,k} \\ & - (N-1) \sum_{i=1}^N \left(\log \sum_{k'=1}^K \exp(\lambda_{i,k'}) + \frac{1}{2} \text{Tr}\{(\text{diag}(\theta(\lambda_i)) - \theta(\lambda_i) \theta(\lambda_i)^T) \nu_i\} \right) \\ & + \sum_{i=1}^N \sum_{j=1}^{i-1} \sum_{k,g=1}^K \phi_{ij,k} \phi_{ji,g} \log P(Y_{ij} | B_{kg}, \sigma_{kg}) + \frac{1}{2} \sum_{i=1}^N \log |\nu_i| - \sum_{i \neq j}^N \sum_{k=1}^K \phi_{ij,k} \log \phi_{ij,k} \end{aligned} \quad (\text{S23})$$

S2. DATASET PREPROCESSING

Chromatin contact files were downloaded from the 4DN consortium data portal [51], and log-observed-over-expected Hi-C maps were extracted from these files using the *hic-straw* [52] Python toolkit. To remove anomalously low reads from the Hi-C maps, we remove all rows and columns where the average value of the normalized Hi-C matrix has a modified Z-score smaller than -3.0 .

ChIP-seq tracks for the input covariates were downloaded from the ENCODE Project database [44], and from these epigenetic data was extracted using the *pyBigWiG* [53] Python toolkit. These tracks were then denoised using a standard lowpass order one Butterworth filter with critical frequency = 0.5 and normalized with a standard scaler.

S3. SIMULATION OF PREDICTED MAPS

Starting from the global model parameter inferred from training data, we can generate predictions for an unseen chromosome with covariate matrix $X^{test} = (x_1^{test}, \dots, x_N^{test})$. In particular, we compute the average membership proportions for each node as:

$$\theta_i^{test} = \Gamma x_i^{test} \quad (\text{S24})$$

Then for the prediction of edge weight Y_{ij}^{test} , we average over all possible pairs of community assignments of nodes i and j , weighting with the membership proportions:

$$Y_{ij}^{test} = \sum_{k,g}^K \theta_{ik} B_{kg} \theta_{jg} \quad (\text{S25})$$

The prediction accuracy is then computed as the Pearson correlation between the model-generated maps and the experimental logarithmic observed over expected Hi-C maps. For modeling the depletion of RAD21 we simply set the row of X^{test} corresponding to RAD21 to zero.

SUPPLEMENTAL TABLE AND FIGURES

Cell Line	Assay	Experiment accession code	Data file code
GM12878	<i>in situ</i> Hi-C	4DNES3JX38V5	4DNFI1UEG1HD
	H3K4me3 (ChIP-seq)	ENCSR057BWO	ENCFF287HAO
	H3K27ac (ChIP-seq)	ENCSR000AKC	ENCFF469WVA
	H3K27me3 (ChIP-seq)	ENCSR000AKD	ENCFF919DOR
	H3K4me1 (ChIP-seq)	ENCSR000AKF	ENCFF564KBE
	H3K36me3 (ChIP-seq)	ENCSR000AKE	ENCFF312MUY
	H3K9me3 (ChIP-seq)	ENCSR000AOX	ENCFF683HCZ
	H3K9ac (ChIP-seq)	ENCSR000AKH	ENCFF599TRR
	H3K4me2 (ChIP-seq)	ENCSR000AKG	ENCFF627OKN
	H4K20me1 (ChIP-seq)	ENCSR000AKI	ENCFF479XIQ
	H2AFZ (ChIP-seq)	ENCSR000AOV	ENCFF935EGN
	H3K79me2 (ChIP-seq)	ENCSR000AOW	ENCFF931USZ
	CTCF (ChIP-seq)	ENCSR000DZN	ENCFF485CGE
	POLR2A (ChIP-seq)	ENCSR000EAD	ENCFF328MMS
	RAD21 (ChIP-seq)	ENCSR000EAC	ENCFF571ZJJ
HCT116	<i>in situ</i> Hi-C	4DNESJV9TH8Q	4DNFILIM6FDL
	H3K4me3 (ChIP-seq)	ENCSR333OPW	ENCFF649ZLF
	H3K27ac (ChIP-seq)	ENCSR661KMA	ENCFF787LMI
	H3K27me3 (ChIP-seq)	ENCFF717ZKL	ENCSR810BDB
	H3K4me1 (ChIP-seq)	ENCFF239FXT	ENCSR161MXP
	H3K36me3 (ChIP-seq)	ENCFF024LGD	ENCSR091QXP
	H3K9me3 (ChIP-seq)	ENCFF254TIW	ENCSR179BUC
	H3K9ac (ChIP-seq)	ENCFF743PJP	ENCSR093SHE
	H3K4me2 (ChIP-seq)	ENCFF693HVA	ENCSR794ULT
	H4K20me1 (ChIP-seq)	ENCSR474DOV	ENCSR474DOV
	H2AFZ (ChIP-seq)	ENCFF863EHT	ENCSR227XNT
	H3K79me2 (ChIP-seq)	ENCFF631DLM	ENCSR494CCN
	CTCF (ChIP-seq)	ENCFF787LAV	ENCSR450DXU
	POLR2A (ChIP-seq)	ENCFF802CGI	ENCSR000EUU
	RAD21 (ChIP-seq)	ENCFF776IXR	ENCSR000BSB

TABLE S1. Accession code for experiments and data files used throughout the paper.

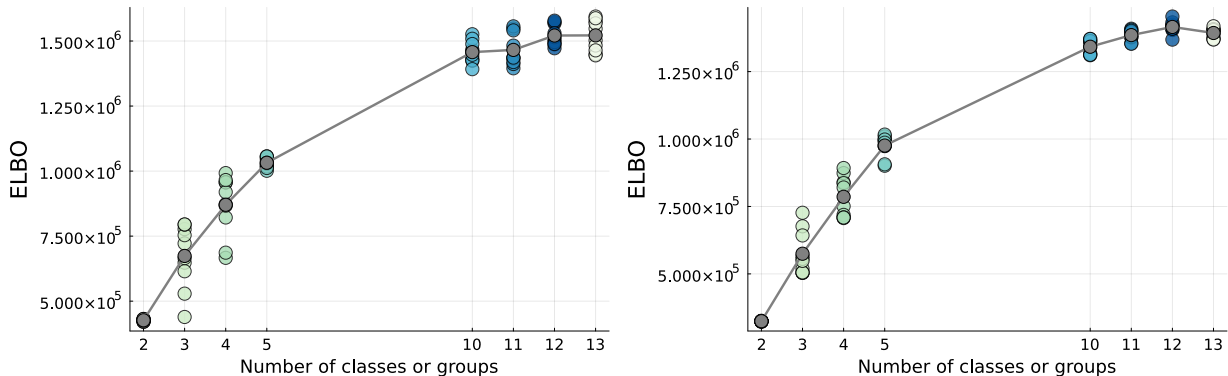


FIG. S1. The Evidence Lower Bound (ELBO) was used as a criterion for Bayesian model selection. The left plot shows ELBO as a function of the number of communities of the model for the training set comprising odd-numbered chromosomes from 11 to 21. The right plot refers to even-numbered chromosomes from 12 to 22. We identify the optimal number of communities as the value where the ELBO peaks or plateaus, leading to the choice $K = 12$.

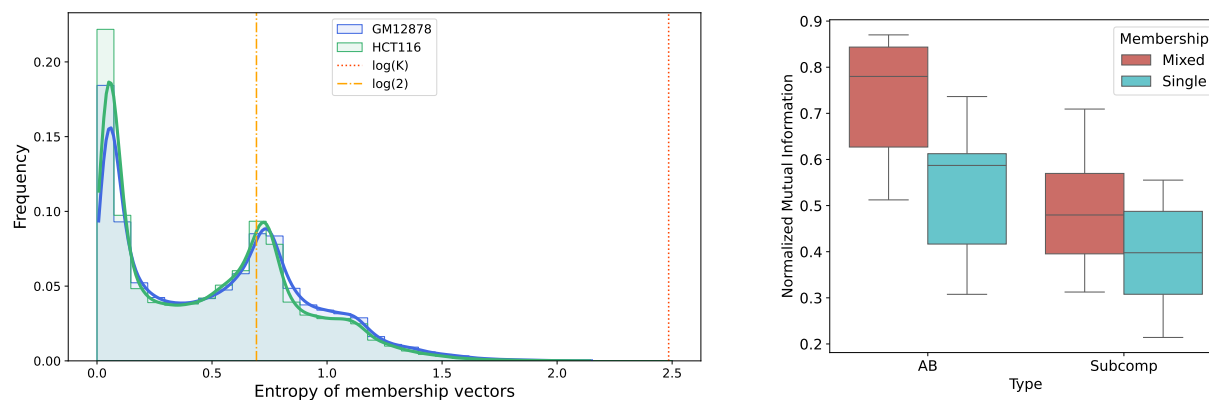


FIG. S2. (Left) Shannon entropies of the MAP estimates of the membership vectors for all the genomic regions under study. The two cell lines that have been studied display a similar distribution of said entropy. In both cases the peak at zero shows that a big fraction of nodes displays a single membership behavior, however, there is still a considerable degree of *mixed-membershipness* if one looks at the entirety of the genomic regions under study. (Right) Normalized Mutual Information (NMI) score between the clustering obtained from the model and the biological annotations. Allowing mixed membership leads to a better recapitulation of the biological annotations.

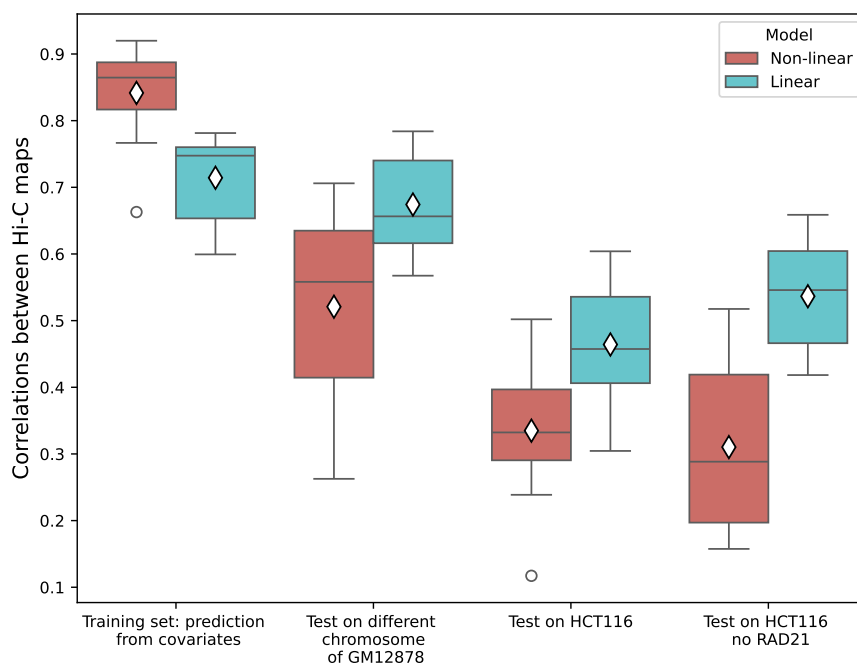


FIG. S3. Correlations between model-generated maps and experimental log O/E Hi-C maps for two models with a different map from biochemical covariates to membership vectors. The turquoise plots correspond to the case where Γ is the simple 14×12 matrix representing a linear mapping, discussed in the main text. The red boxes correspond to the case where $\Gamma(\cdot)$ is a feed-forward deep neural network with 4 hidden layers of size (64, 64, 64, 32) with the standard *ReLU* (rectified linear unit) non-linear activations. While on the training set, the non-linear model better reproduces experimental contact maps, already for test chromosomes on the same cell-line the correlations decrease drastically.